Available online at www.sciencedirect.com
SCIENCE DIRECT®
International Journal of Heat and Mass Transfer 48 (2005) 5549–5562
International Journal of HEAT and MASS TRANSFER
www.elsevier.com/locate/ijhmt

Identification of boundary heat fluxes in a falling film experiment using high resolution temperature measurements

Sven Groß [a], Marcus Soemers [a], Adel Mhamdi [b], Faruk Al Sibai [c], Arnold Reusken [a], Wolfgang Marquardt [b,*], Ulrich Renz [c]

[a] *Numerical Mathematics, RWTH Aachen University, Lehrstuhl für Numerische Mathematik, Templergraben 55, D-52056 Aachen, Germany*
[b] *Process Systems Engineering, RWTH Aachen University, Lehrstuhl für Prozesstechnik, Turmstraße 46, D-52064 Aachen, Germany*
[c] *Heat Transfer and Air Conditioning, RWTH Aachen University, Lehrstuhl für Wärmeübertragung und Klimatechnik, Eilfschornsteinstraße 18, D-52056 Aachen, Germany*

Received 25 October 2004; received in revised form 31 May 2005
Available online 1 September 2005

Abstract

In this paper, we consider a three-dimensional inverse heat conduction problem (IHCP) in a falling film experiment. The wavy film is heated electrically by a thin constantan foil and the temperature on the back side of this foil is measured by high resolution infrared (IR) thermography. The transient heat flux at the inaccessible film side of the foil is determined from the IR data and the electrical heating power. The IHCP is formulated as a mathematical optimization problem, which is solved with the conjugate gradient method. In each step of the iterative process two direct transient heat conduction problems must be solved. We apply a one step θ-method and piecewise linear finite elements on a tetrahedral grid for the time and space discretization, respectively. The resulting large sparse system of equations is solved with a preconditioned Krylov subspace method. We give results of simulated experiments, which illustrate the performance and tuning of the solution method, and finally present the estimation results from temperature measurements obtained during falling film experiments.

Keywords: Inverse problem; Regularization; Conjugate gradient method; Falling film; Heat flux estimation; Anisotropic finite elements; Model-based experimental analysis

1. Introduction

The modeling of kinetic phenomena in multiphase systems leads to problems of model structure and parameter identification, which belong to the class of inverse problems [18]. Challenging inverse problems appear in the study of heat and mass transfer mechanisms in falling films, which are of special interest, due to their technical relevance in industry.

Many investigations have already been performed to analyze the heat and mass transfer in falling films [10,11,15,17]. It has been observed that both, heat and mass transfer in wavy films are significantly higher than

* Corresponding author. Tel.: +49 241 8096712; fax: +49 241 8092326.
E-mail address: marquardt@lpt.rwth-aachen.de (W. Marquardt).

0017-9310/$ - see front matter © 2005 Elsevier Ltd. All rights reserved.
doi:10.1016/j.ijheatmasstransfer.2005.06.030

Nomenclature

Direct problems

Ω	3D heating foil
Γ_1, Γ_2	back and film side of Ω
Γ_r	remaining boundary of Ω
n	outer normal on $\partial\Omega$
T	(continuous) temperature distribution
T_0	initial temperature distribution
T_m	measurement data
q_h	heat flux modeling electrical heating
q_c	unknown surface heat flux
t_0, t_f	initial and final times
t_b	time backwards
ρ, c, λ	density, specific heat and heat conductivity
a	thermal diffusivity
ψ	adjoint problem solution
S	sensitivity problem solution

Optimization

$\|\cdot\|_{L_2}$	residual norm
$(\cdot,\cdot)$	$L_2(\Omega)$ scalar product
J	objective functional
∇J	gradient of the objective functional
p^n	descent direction (nth iteration)
γ^n	conjugate coefficient (nth iteration)
μ^n	step length in search direction (nth iteration)

Discretization

$H^1(\Omega)$	Sobolev space
V, V_h	function and finite element space
α, β	functionals in the weak formulation
$\{\varphi_i\}_{1 \leqslant i \leqslant N}$	standard nodal basis of V_h
T_h, T_h^k	semi-discrete and fully discrete temperatures
$\mathcal{T}$	triangulation of Ω
θ	implicitness parameter
τ	time step size
M, A	mass and stiffness matrices

Simulation examples

n_t	number of time steps applied
n_{opt}	number of optimization steps applied
q_c^{ex}	given exact heat flux
T_m^{ex}	generated measurement data
ϵ	threshold parameter
ω, σ	measurement error and standard deviation
A_1	surface of Γ_1
κ	regularization parameter

those predicted by the Nusselt solution. In these studies semi-empirical correlations of the heat and mass transfer enhancement have been presented, however, the mechanisms of the transport processes and the flow characteristics of wavy films have not been fully explained.

In this paper, we focus on the heat transfer in falling films. It is influenced by the film thickness and the wave structure. In the substrate region, heat transfer is dominated by conduction, whereas in the in wave region, the heat is transferred by convection, too. To analyze the influence of the wave characteristics of thin films on the heat transfer, measurements were carried out in a falling film apparatus specifically designed for this purpose. Fig. 1 shows the schematic representation of the experiment used in this research. It consists of a fluid cycle with a loudspeaker to produce 2D-waves with a certain frequency. The laminar wavy falling film travels along one side of a thin foil heated electrically via a DC power supply. To take temperature measurements on the foil back side with high resolution in space and time, we use an infrared camera CEDIP Jade II [1,14]. It has a HgCdTe focal-plane-array with a resolution of 320×240 pixel and is sensitive to radiation in the long wavelength range between 7.7 and 9.5 μm.

The identification problem of estimating the heat flux on the film surface is coupled with the fluid dynamics of the falling film. This coupling results in an inverse problem of very high complexity. In this paper, a simplified, but still challenging and interesting problem is considered, where the heat transfer is decoupled from the fluid dynamics. We investigate the unsteady heat transfer from the heating foil to the falling film.

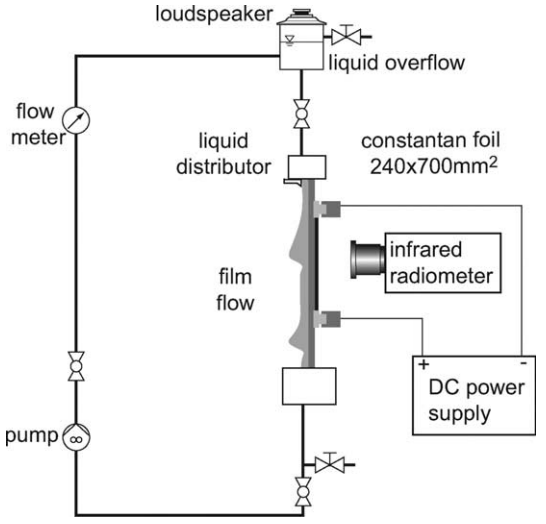

Fig. 1. Schematic representation of the falling film experiment.

Temperature measurements are used to estimate the heat flux on the film side of the foil as a function of space and time with the remaining initial and boundary conditions assumed to be known. This is a model-free estimation problem, since no further assumptions on the heat transfer mechanism are made. In subsequent steps the estimated heat flux can be correlated with other quantities in the falling film such as the mean film temperature and the flow regime to obtain a better understanding of the related kinetic phenomena. The goal is not only the solution of this particular inverse heat transfer problem, but also to gain a better understanding of solution methods for multidimensional non-linear inverse problems in multiphase flow systems. Such an understanding is essential as a basis for future investigations of more complex inverse transport problems such as heat transfer through the falling film, mass transfer from the film to the gas phase, or reaction inside the film.

The inverse heat conduction problem considered consists of determining the heat flux $q_c(\mathbf{x},t)$ on the film side of the foil Γ_2 from measurement data T_m, which are taken on the foil back side Γ_1. These measurements are clearly influenced by the transport phenomena in the falling film and by the surface wave pattern. Fig. 2 shows the schematic representation of the three-dimensional plate $\Omega \subset \mathbb{R}^3$ with heat transfer on Γ_2. There are two alternatives for modeling the electrical heating at the back side of the thin constantan foil. We could consider a volumetric source term in the heat conduction equations or—as done in this paper—we could assume that we have a constant boundary heat flux on Γ_1 as shown in Fig. 2.

Many studies related to IHCPs have already been published (cf. [2,5] and the references therein). Most literature on numerical solution methods is restricted to one or two space dimensions. For problems in three space dimensions only few publications are available [6,12,23]. In these papers only simulated data with few point-wise measurement locations have been used. Recently, an efficient method for the solution of transient 3D IHCPs has been published and applied to experimental investigations of pool boiling [16]. In contrast to this filter-based method of limited space–time resolution, we investigate in this work an optimization-based solution of the 3D IHCP for the reconstruction of boundary heat fluxes with high resolution in space and time employing high resolution spatio–temporal temperature measurements. Although the problem geometry is simple, there is a numerical complication caused by the plate thickness (25 μm), which is very small compared to its other dimensions. Due to this geometric anisotropy one has to be careful in the choice of the solution methods for the direct problems.

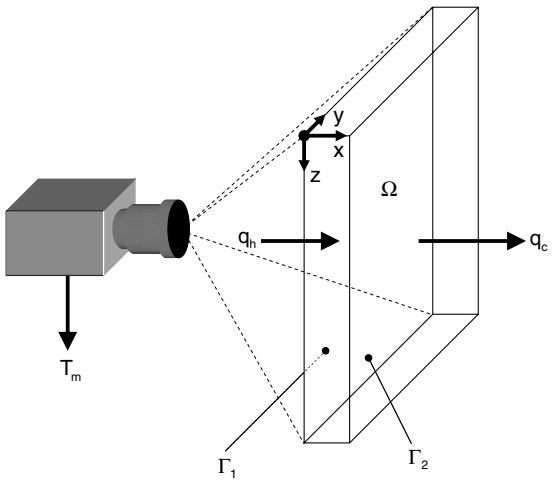

Fig. 2. Schematic representation of the 3D heating foil.

The paper is organized as follows. The inverse problem is formulated as an optimization problem in Section 2. In Section 3, the solution method based on conjugate gradients (CG) is introduced. The solution methods for the direct problems occuring in the optimization procedure are discussed in Section 4. Some test examples for the validation of the IHCP solver are presented in Section 5, while results employing experimental measurement data are given in Section 6. Section 7 contains some conclusions and remarks concerning future work.

2. Formulation of the inverse problem

We consider the domain Ω shown in Fig. 2 with boundary $\partial\Omega = \Gamma_1 \cup \Gamma_2 \cup \Gamma_r$, where Γ_1, Γ_2 and Γ_r denote the measurement side, the film side and the remaining boundaries of the heating foil. The *direct problem* consists of the following heat conduction equation for the temperature T

$$\frac{\partial T}{\partial t}(\mathbf{x},t) = a\Delta T(\mathbf{x},t), \quad (\mathbf{x},t) \in \Omega \times [t_0, t_f], \tag{1}$$

$$T(\mathbf{x},t_0) = T_0(\mathbf{x}), \quad \mathbf{x} \in \Omega, \tag{2}$$

$$-\lambda \frac{\partial T}{\partial n}(\mathbf{x},t) = q_h(\mathbf{x},t), \quad (\mathbf{x},t) \in \Gamma_1 \times [t_0, t_f], \tag{3}$$

$$-\lambda \frac{\partial T}{\partial n}(\mathbf{x},t) = q_c(\mathbf{x},t), \quad (\mathbf{x},t) \in \Gamma_2 \times [t_0, t_f], \tag{4}$$

where T_0, q_h and q_c are the initial and boundary conditions, respectively. The outer normal on the boundary is denoted by n. The initial and final times are denoted by t_0 and t_f, respectively. The known material properties density ρ, specific heat capacity c and heat conductivity λ enter the thermal diffusivity $a = \frac{\lambda}{\rho c}$, which is assumed to be constant, since the experimental temperature range is very small. In this paper, the boundary conditions, which are not given explicitly, are assumed to be zero, i.e. $-\lambda \frac{\partial T}{\partial n}(\mathbf{x},t) = 0$, $(\mathbf{x},t) \in \Gamma_r$.

The *inverse problem* corresponds to the estimation of the heat flux q_c on Γ_2 on the basis of suitable measurement data T_m on Γ_1, under the assumption that the values of T_0 and q_h are known. This is a typical example of an inverse heat conduction problem.

In this work we consider an optimization-based formulation, since it can easily be adapted to more complex situations. The unknown quantity q_c is determined such that

$$J(q_c) := \frac{1}{2}\|T(\mathbf{x},t;q_c)_{|\Gamma_1} - T_m(\mathbf{x},t)\|^2_{L_2} \to \min$$
$$\text{s.t. Eqs. (1)–(4).} \tag{5}$$

To emphasize the dependence of T on the boundary heat flux q_c we refer to the solution of (1)–(4) as $T(\mathbf{x},t;q_c)$. The corresponding norm in (5) is defined by

$$\|\cdot\|^2_{L_2} := \int_{t_0}^{t_f}\int_{\Gamma_1}(\cdot)^2\,d\mathbf{x}\,dt. \tag{6}$$

Regularization [7] is only introduced via the discretization and suitable stopping criteria for the optimization algorithm. This strategy is discussed below in more detail. An alternative approach is to add a regularizing term $R(q_c)$ to the objective function J, which penalizes the variation of q_c. This method will be considered in future work.

3. Minimization algorithm

For the solution of the least squares problem (5) many methods are available [2,3,7]. Here, we use the *conjugate gradient (CG) method* (see [7,20] for details), which is very efficient in terms of the number of iterations compared to other semi-iterative methods, if the discrepancy principle is chosen as a stopping rule [7]. For non-linear problems, some variants of this algorithm are available in the literature [20].

The CG method solves the minimization problem by setting up an iteration sequence for the unknown function q_c (see Fig. 3). Here, the solution at iteration n is updated from the previous one until some stopping conditions are fulfilled. For the determination of the search direction the conjugate gradient method is used, which requires the gradient of the functional (5) to compute the search direction. The gradient is defined as the first order Fréchet derivative of the functional at some point $q_c \in W$, where W is a suitable function space. We consider the space W of continuous and piecewise linear functions on Γ_2 which is due to the discretization of the domain Ω with P1-elements on a tetrahedral grid. If the functional increment at some point q_c is given by

$$J(q_c+\delta q_c) - J(q_c) = \int_{t_0}^{t_f}\int_{\Gamma_2}\nabla J(\mathbf{x},t)\delta q_c(\mathbf{x},t)\,d\mathbf{x}\,dt + o(\|\delta q_c\|) \tag{7}$$

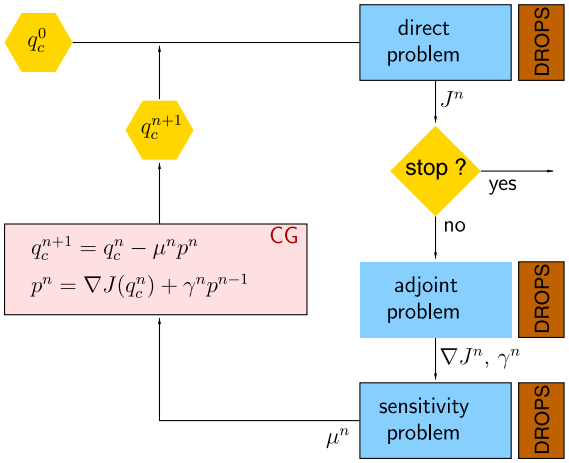

Fig. 3. CG method—iterative procedure.

with $q_c + \delta q_c \in W$, then the function $\nabla J(\mathbf{x},t)$ is the *functional gradient* at q_c.

The CG procedure, illustrated in Fig. 3, comprises the following calculation steps:

(i) Set $n = 0$ and choose a starting value $q_c^0 \in W$, e.g. $q_c^0 \equiv 0$.

(ii) Calculate the objective function. If the convergence conditions are satisfied stop, otherwise continue.

(iii) Calculate the new search direction $p^n = \nabla J(q_c^n) + \gamma^n p^{n-1}$. The gradient $\nabla J(q_c^n)$ is obtained from the solution of the *adjoint problem* (cf. Section 3.1). The *conjugate coefficient* γ^n, $n \geqslant 1$, is determined from

$$\gamma^n = \frac{\int_{t_0}^{t_f}\int_{\Gamma_2}[\nabla J(q_c^n)]^2\,d\mathbf{x}\,dt}{\int_{t_0}^{t_f}\int_{\Gamma_2}[\nabla J(q_c^{n-1})]^2\,d\mathbf{x}\,dt} \tag{8}$$

and $\gamma^0 = 0$.

(iv) Calculate the step length along the search direction by solving the one-dimensional optimization problem

$$\mu^n = \operatorname{argmin}_{\mu\geqslant 0} J(q_c^n - \mu p^n). \tag{9}$$

In our case μ^n is given by

$$\mu^n = \frac{\int_{t_0}^{t_f}\int_{\Gamma_1}[T(\mathbf{x},t;q_c^n) - T_m(\mathbf{x},t)]S(\mathbf{x},t)\,d\mathbf{x}\,dt}{\int_{t_0}^{t_f}\int_{\Gamma_1}[S(\mathbf{x},t)]^2\,d\mathbf{x}\,dt}, \tag{10}$$

with S being the solution of the *sensitivity problem* (cf. Section 3.2).

(v) Update the approximation

$$q_c^{n+1} = q_c^n - \mu^n p^n. \tag{11}$$

Increase n by one and go back to (ii).

Two difficulties arise in applying this solution approach. First we have to calculate the functional gradient and second we have to solve the optimization problem in (9) to find a step length along the descent direction. In the next section we discuss these two issues.

3.1. Adjoint problem

In the iterative gradient-based procedure, we need the gradient $\nabla J(\mathbf{x},t)$ to calculate the descent direction p^n. It can be shown that the identity

$$\nabla J(\mathbf{x},t) = \psi(\mathbf{x},t)|_{\Gamma_2} \tag{12}$$

holds, where the adjoint variable ψ is the solution of the *adjoint problem*

$$\frac{\partial \psi}{\partial t}(\mathbf{x},t) = -a\Delta\psi(\mathbf{x},t), \quad (\mathbf{x},t) \in \Omega \times [t_0,t_f], \tag{13}$$

$$\psi(\mathbf{x},t_f) = 0, \quad \mathbf{x} \in \Omega, \tag{14}$$

$$-\lambda\frac{\partial \psi}{\partial n}(\mathbf{x},t) = [T(\mathbf{x},t;q_c) - T_m(\mathbf{x},t)], \quad (\mathbf{x},t) \in \Gamma_1 \times [t_0,t_f], \tag{15}$$

$$-\lambda\frac{\partial \psi}{\partial n}(\mathbf{x},t) = 0, \quad (\mathbf{x},t) \in \Gamma_2 \times [t_0,t_f]. \tag{16}$$

We do not give a derivation of the identity in (12) since it follows from standard procedures [2]. For the adjoint problem, there is no initial condition, but rather a condition at final time t_f. By introducing a new time variable $t_b = t_f - t$, we get an equation system which has the same structure as the original direct problem (1)–(4), however, with different initial and boundary conditions.

3.2. Sensitivity problem

The step length μ^n along the search direction p^n is obtained from the solution of the *sensitivity problem* given by

$$\frac{\partial S}{\partial t}(\mathbf{x},t) = a\Delta S(\mathbf{x},t), \quad (\mathbf{x},t) \in \Omega \times [t_0,t_f], \tag{17}$$

$$S(\mathbf{x},t_0) = 0, \quad \mathbf{x} \in \Omega, \tag{18}$$

$$-\lambda\frac{\partial S}{\partial n}(\mathbf{x},t) = 0, \quad (\mathbf{x},t) \in \Gamma_1 \times [t_0,t_f], \tag{19}$$

$$-\lambda\frac{\partial S}{\partial n}(\mathbf{x},t) = p^n(\mathbf{x},t), \quad (\mathbf{x},t) \in \Gamma_2 \times [t_0,t_f]. \tag{20}$$

Again, it has the same structure as the direct problem (1)–(4), but with different initial and boundary conditions.

In the iterative process, three direct heat conduction problems, the *direct*, *adjoint* and *sensitivity* problems, have to be solved. To calculate the corresponding solutions the same software code can be used, since all of the mentioned problems have the same structure. In many publications on the CG method, the three direct problems are solved at each iteration. Actually, in the particular case of linear problems only the solutions of *two* direct problems are needed in each optimization iteration (see Fig. 3). In fact, using the linearity, the temperature can be computed from the identity

$$T(q_c^{n+1}) = T(q_c^n) - \mu^n S, \tag{21}$$

where S is the solution of the *sensitivity problem* (17)–(20). So the *direct problem* (1)–(4) is solved only once at the very beginning (i.e. $n = 0$). This results in a substantial reduction of the computational time.

4. Solution of the direct problems

The solution of the direct 3D heat conduction equations is computed using the software package DROPS (cf. [8]), which is based on multilevel nested grids and finite element discretization methods. Some aspects of the numerical methods implemented in DROPS are briefly described in this section. For the time discretization, a standard one step θ-method is used [19]. Piecewise linear finite elements on a tetrahedral grid are employed for the space discretization [21]. The resulting discrete systems of equations are solved with a preconditioned Krylov subspace method.

We outline the finite element method that is used for the *space discretization*. It is based on a variational formulation of the direct problem: For $t \in [t_0,t_f]$ find $T(t) \in V$ such that

$$\left(\frac{\partial T(t)}{\partial t}, v\right) + (a\nabla T(t), \nabla v) = -\frac{a}{\lambda}\int_{\partial\Omega} qv\,d\sigma \quad \forall v \in V. \tag{22}$$

Here V is a suitable function space (the Sobolev space $H^1(\Omega)$) and $(u,v) := \int_\Omega u \cdot v\,d\mathbf{x}$ denotes the $L_2(\Omega)$ scalar product. For notational convenience we introduce the bilinear form $\alpha(u,v) := (a\nabla u, \nabla v)$ and the functional $\beta(t;v)$ which is defined by the right hand side in (22). The variational problem can be rewritten in compact form as

$$\left(\frac{\partial T(t)}{\partial t}, v\right) + \alpha(T(t),v) = \beta(t;v) \quad \forall v \in V.$$

For the discretization we use a triangulation $\mathcal{T}$ of Ω which consists of tetrahedra. The finite element space $V_h \subset V$ consists of continuous piecewise linear functions. The degrees of freedom are located at the vertices of the tetrahedra. Let $\{\varphi_i\}_{1 \leqslant i \leqslant N}$ be the standard nodal basis of the space V_h. The discrete problem is then given as follows: Find $T_h \in V_h$ such that

$$\left(\frac{\partial T_h(t)}{\partial t}, \varphi_i\right) + \alpha(T_h(t),\varphi_i) = \beta(t;\varphi_i) \quad \forall 1 \leqslant i \leqslant N. \tag{23}$$

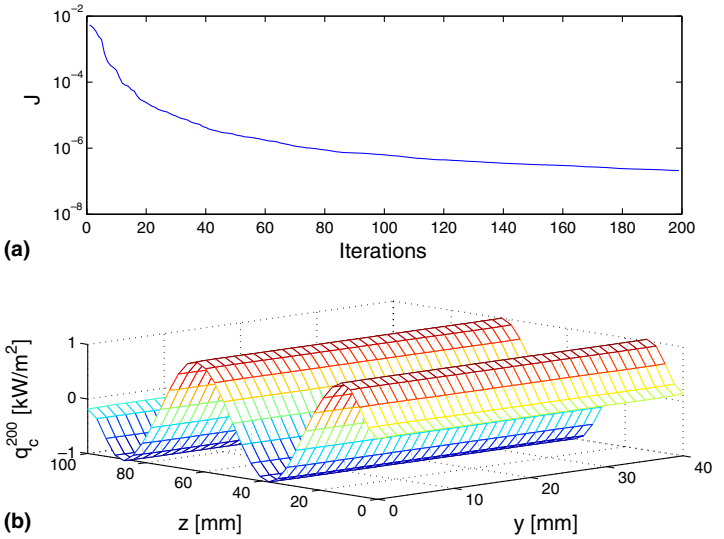

Fig. 4. (a) Objective functional and (b) estimated heat flux q_c^{200}.

This is a system of coupled ordinary differential equations. For the *time discretization* a one step θ-scheme is applied. The time step size is denoted by τ and the approximate solution at time t_k is denoted by T_{h}^k. Then given T_{h}^k, we get the approximate solution $T_{\mathrm{h}}^{k+1} \approx T(t_{k+1},\cdot)$ by solving the problem

$$\begin{aligned}(T_{\mathrm{h}}^{k+1},\varphi_i) &+ \theta\tau\alpha(T_{\mathrm{h}}^{k+1},\varphi_i)\\ &= (T_{\mathrm{h}}^{k},\varphi_i) - (1-\theta)\tau\alpha(T_{\mathrm{h}}^{k},\varphi_i) + \theta\tau\beta(t_{k+1};\varphi_i)\\ &\quad + (1-\theta)\tau\beta(t_k;\varphi_i), \quad \forall 1 \leqslant i \leqslant N. \end{aligned} \tag{24}$$

The parameter $0 \leqslant \theta \leqslant 1$ controls the implicitness of the scheme. In particular, $\theta = 0$ yields the explicit Euler scheme, $\theta = 1$ the implicit Euler scheme and $\theta = 0.5$ leads to the Crank–Nicholson scheme. Because of the strong stiffness of the system in (23) only implicit schemes ($\theta \neq 0$) should be used to solve the instationary heat conduction problems. The implicit Euler scheme is only first order accurate (i.e. the discretization error is $\mathcal{O}(\tau)$), but is strongly A-stable. The Crank–Nicholson scheme is of order two, is A-stable, but does not have the strong A-stability property, which may lead to stability problems in certain situations. In the remainder of this paper we only consider $\theta = 0.5$ and $\theta = 1$.

Let $\mathbf{u} \in \mathbb{R}^N$ be the coefficient vector of the representation of $T_{\mathrm{h}} = \sum_{i=1}^N u_i\varphi_i$ in the nodal basis. Eq. (24) then represents a linear system of equations for the unknown function T_{h}^{k+1}, which can be written as

$$[M + \theta\tau A]\mathbf{u}^{k+1} = [M - (1-\theta)\tau A]\mathbf{u}^k + \theta\tau\mathbf{b}^{k+1} + (1-\theta)\tau\mathbf{b}^k.$$

Here M denotes the mass matrix and A the stiffness matrix

$$M_{\mathrm{ij}} := (\varphi_j,\varphi_i), \quad A_{\mathrm{ij}} := \alpha(\varphi_j,\varphi_i)$$

and $\mathbf{b}^k$, $\mathbf{b}^{k+1}$ are the right hand sides with

$$\mathbf{b}_i^k = \beta(t_k;\varphi_i), \quad \mathbf{b}_i^{k+1} = \beta(t_{k+1};\varphi_i).$$

The system matrix $M + \theta\tau A$ is symmetric positive definite, thus a preconditioned conjugate gradient (PCG) method can be applied to solve this system of linear equations [22]. For the simulations presented in this paper we use the SSOR method for preconditioning.

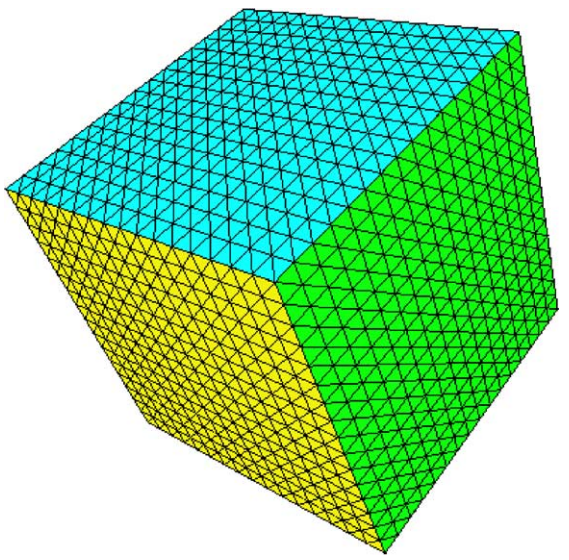

Fig. 5. Triangulation of the unit cube.

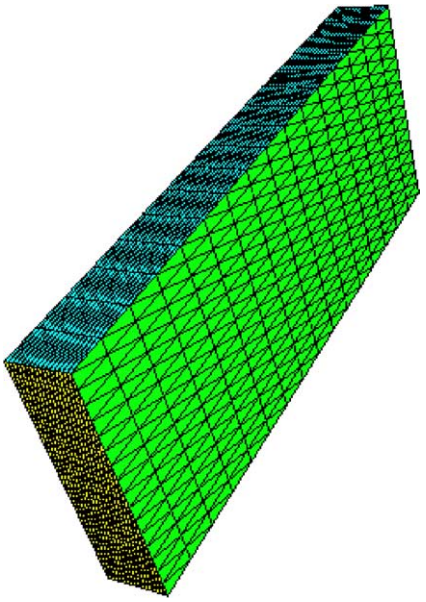

Fig. 6. Triangulation of a geometrical anisotropic domain.

At the end of this section, we briefly comment on the performance of the developed solver, because we consider a very thin heating foil. In this context we mention the properties of the applied triangulation technique and the arising degenerated tetrahedra (see Fig. 5 and 6). The standard kind of triangulation used within the software package DROPS avoids large angles inside the faces as well as between two faces of each tetrahedron, independent of the geometry dimension (for more information see [8]). Taking into consideration the so-called *maximum angle principle* (see [4,13]) we do not expect a loss of quality with respect to the discretizations of the involved direct heat conduction problems in the case of increasing anisotropy. This is confirmed by numerical experiments. However, we expect that the efficiency of the PCG solver decreases with increasing geometrical degeneracy, which has been observed in numerical experiments, too. In this paper, we will not analyze these observations in more detail.

5. Simulation examples for method and code validation

The DROPS code as well as the optimization method were validated via various simulations. Some results of these case studies are given in this section. Results obtained with experimental data are presented in the next section.

In the following simulations, we applied the implicit Euler scheme for the time discretization to avoid stability problems. However, a comparison with the second order Crank–Nicholson scheme showed no substantial differences with respect to the quality of the obtained heat flux estimations. The material properties chosen in this section do not reflect the real experimental data of Section 6 as we focus on method and code validation.

5.1. Example 1: continuous and time varying heat flux

In Examples 1 and 2, we consider the domain $\Omega := 10 \times 40 \times 100\,\mathrm{mm}^3$. The material properties for these cases are lumped in the parameter $a = 10^{-4}\,\mathrm{m}^2/\mathrm{s}$. For the time discretization (implicit Euler scheme) we use the time step size $\tau = 0.01\,\mathrm{s}$ and apply 200 time steps. The initial and known boundary conditions consist of a constant temperature distribution $T(x, t_0) = 20\,^\circ\mathrm{C}$, $\mathbf{x} \in \Omega$, a constant heat flux $q_\mathrm{h}(\mathbf{x}, t) = 2\,\mathrm{kW/m}^2$, $(\mathbf{x}, t) \in \Gamma_1 \times [t_0, t_\mathrm{f}]$ for heat addition and perfectly insulated boundaries on Γ_r (cf. the notation of Section 2). For the initialization of the optimization procedure, we choose $q_c^0(\mathbf{x}, t) = 0$, $(\mathbf{x},t) \in \Gamma_2 \times [t_0, t_\mathrm{f}]$ (see Fig. 3).

In this first example, a uniform space discretization with 35,937 unknowns is applied (corresponding to an initial grid triangulation with $32 \times 32 \times 32$ parallelepipeds and 196,608 tetrahedra, for more details cf. [8]). As a basis of this simulation, we choose a shape of the heat flux, which represents an intuitive approximation of the real quantity in the falling film experiment. This heat flux is denoted by $q_c^\mathrm{ex}(\mathbf{x}, t)$, $(\mathbf{x}, t) \in \Gamma_2 \times [t_0, t_\mathrm{f}]$ and has a sinusoidal pattern over the space coordinate in the flow direction of the falling film (i.e. the z-direction). The wavy pattern is assumed to be time dependent, such that the waves travel along the z-direction over time

$$q_c^\mathrm{ex}(x, y, z, t) = \sin\left(4\pi\left(\frac{z}{100} + \frac{t}{200}\right)\right),$$
$$(x, y, z) \in \Gamma_2, \quad t \in [t_0, t_\mathrm{f}].$$

5.1.1. Estimation with error-free measurements

First, we present the estimation results of the boundary heat flux with error-free measurements. As measurement data, we take the temperature T_m^ex obtained from the solution of the direct heat conduction problem with the chosen quantity q_c^ex as the corresponding boundary condition on Γ_2.

In Fig. 4(a), the objective functional is plotted over the number of optimization iterations, whereas a snapshot (at one point in time) of the estimated heat flux at the end of the optimization is presented in Fig. 4(b). We observe the well known convergence behavior of the applied CG method in terms of a more rapid decrease of the objective functional at the beginning of the iterative process followed by stagnation at a certain level. Plot (b) shows that the estimated heat flux is, like the exact quantity, constant in the y-direction. Therefore, we restrict the following plots to a cut through the y-axis to look at the estimation quality in more detail.

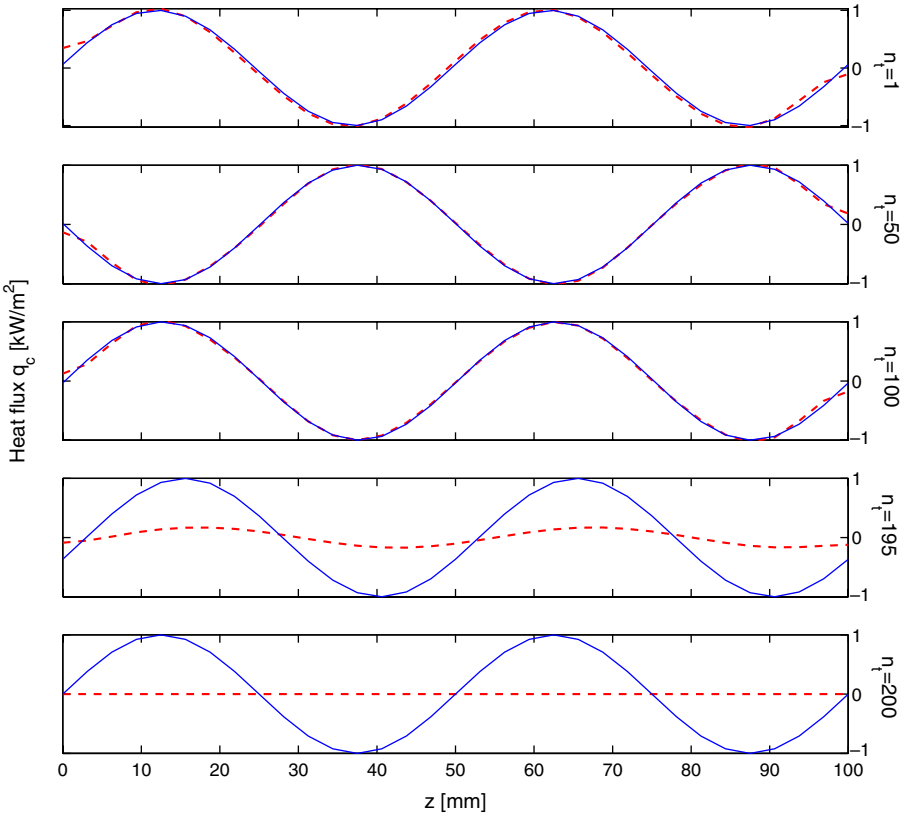

Fig. 7. Exact heat flux q_c^{ex} (solid line) and estimated heat flux q_c^{200} (dashed line) for different time steps n_t.

Both exact and estimated heat fluxes are given in Fig. 7 over the z-direction for constant $y = 20$ mm (i.e. in the middle of the y-coordinate) and different numbers of time steps applied, which are denoted by n_t. Except for a region at final time the recovered heat flux is of high quality, since there are only little visible deviations compared to the exact quantity. At final time, the estimation quality decreases, due to the fact that the solution of the adjoint problem (i.e. the gradient of the objective functional) is zero and therefore causes no improvement of the start approximation for $t = t_f$. The effect of the iterative CG method is presented in Fig. 8. Here the error free and estimated heat fluxes are shown at the fixed time level $n_t = 100$ and different iterations of the optimization, which are denoted by n_{opt}. We clearly observe that the estimation quality increases with a rising number of optimization steps, since we use error-free temperature measurements. To stop the iterations, we consider the usual procedure and specify a small threshold parameter ϵ for the objective function, i.e.

$$J(q_c^n) < \epsilon. \tag{25}$$

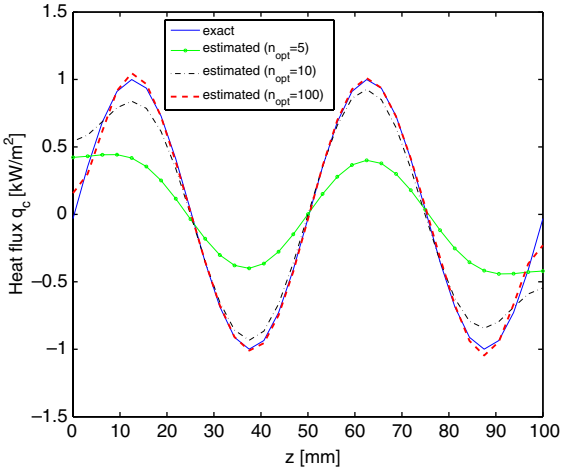

Fig. 8. Estimated heat flux for different optimization iterations n_{opt}.

We see from Fig. 4(a) that about 80 iterations are needed to satisfy the stopping rule (25) with $\epsilon = 10^{-6}$. Clearly, smaller values of ϵ lead to more iterations.

5.1.2. Estimation in the presence of measurement errors

In this section, we perturb the exact temperature T_m^{ex}, obtained as described in the previous section, using an artificial measurement error ω. We assume the perturbed temperature T_m given by

$$T_m = T_m^{ex} + \sigma\omega,$$

with σ being the standard deviation of the measurement error. The values of ω are generated from a zero mean normal distribution with variance one. The parameter σ is used to control the error amount added to the exact data. In the case of measurement errors, we cannot expect that the objective functional becomes arbitrarily small. To find an appropriate ϵ to stop the iterations, we can use known parameter choice rules from the inverse problems literature [7].

The discrepancy principle suggests that we stop the iterations, when the residual approximately equals σ. From (5), we get the expression

$$\epsilon = \frac{1}{2}\kappa(t_f - t_0)A_1\sigma^2,$$

for the threshold parameter ϵ in (25), where A_1 is the surface of Γ_1 and $\kappa > 1$ is a parameter. In the following simulations we used $\kappa = 1.02$. A detailed discussion of this method is given in [7]. For $\sigma = 0.25$ we obtain the optimal result after $n_{opt} = 40$ iterations using the stopping rule above. The estimates and the corresponding temperatures are given in Fig. 9. A good reconstruction of the exact heat flux is achieved. By performing further iterations, the estimated heat flux begins to oscillate and the estimation quality decreases. Similar results have been obtained with higher values of the noise level σ.

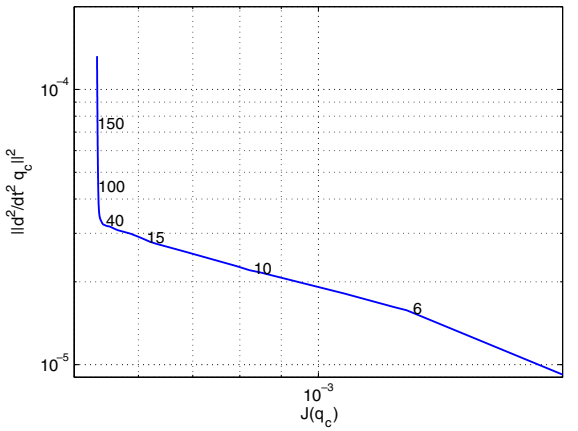

Fig. 10. L-curve for perturbed measurements with $\sigma = 0.25$.

An alternative stopping criterion is to use heuristic rules such as the L-curve [9], which is a parameterized plot of the residual against a solution norm. For $\sigma = 0.25$, the L-curve is shown in Fig. 10. The best compromise is found at the point of the L-curve with maximum curvature. For the considered case, the optimal value is about $n_{opt} = 40$ iterations, i.e. the result is comparable to the one obtained by the discrepancy principle.

5.2. Example 2: discontinuous and steady state heat flux

In this section, we present a simulation based on a heat flux q_c^{ex} that is time independent and discontinuous

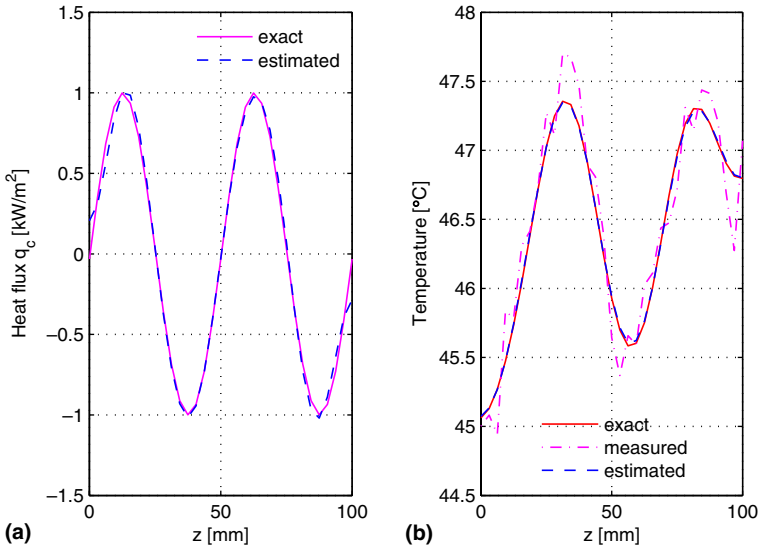

Fig. 9. Estimated heat flux with perturbed measurements $\sigma = 0.25$: (a) exact and estimated heat flux q_c for $n_{opt} = 40$ and (b) exact, measured and estimated temperature.

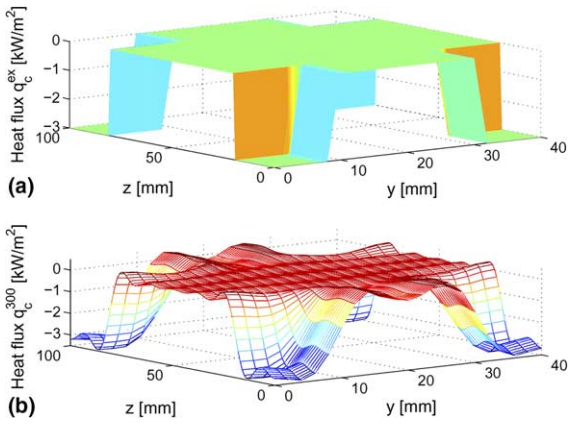

Fig. 11. Exact (a) and estimated (b) heat flux.

on Γ_2. Thus this heat flux does not belong to the Sobolev space $H^1(\Omega)$. It has the representation

$$q_c^{\mathrm{ex}}(x,y,z;t) = \begin{cases} 0 & \text{for } (x,y,z) \in \Gamma_0, \\ -3\ \mathrm{kW/m^2} & \text{else,} \end{cases}$$

with $\Gamma_0 := \{(x,y,z) \in \Gamma_2 | y \in [10,30] \vee z \in [20,80]\}$ (see Fig. 11(a)).

We again consider the situation described in the first paragraph of Example 1, but this time we use a quasi-uniform discretization with 36,057 unknowns (corresponding to an initial triangulation with $16 \times 20 \times 100$ parallelepipeds with respect to the space coordinates). We consider these data with focus on the real falling film experiment, where we choose a fine space discretization (resolution) in the flow direction (z-coordinate) and relatively coarse resolutions in the other directions (see Section 6).

The obtained estimation result is given in Fig. 11(b). The objective functional shows the same typical behaviour as already described in Example 1 and therefore we do not give the plot here. Both, exact and estimated solutions of the inverse problem are given in Fig. 12(a) and (b) for cuts along the z-axis and the y-axis respectively ($y = 0$ and $z = 0$). Again, results for different iteration numbers of the optimization procedure are shown.

Due to the discontinuities of the error free boundary heat flux, oscillations appear in the piecewise continuous approximations with an increasing number of optimization iterations applied. A comparison of both plots with 100 (a) and 20 (b) unknowns in the corresponding space directions respectively shows a better approximation quality for the case with higher space resolution.

The number of unknowns needed to reach the desired accuracy should be kept as small as possible for efficiency reasons. Instead of refining the whole grid, it may be better to use locally refined grids. Local grid refinement leads to good approximation properties, while at the same time the number of unknowns is severely decreased

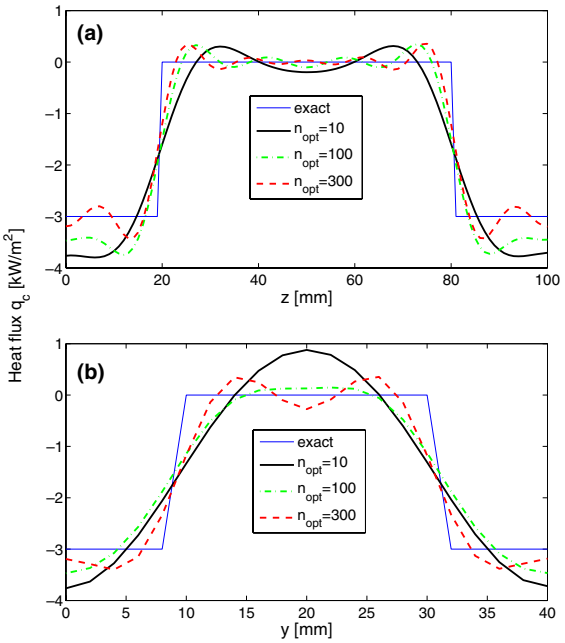

Fig. 12. 2D plots of the heat fluxes for $y = 0$ (a) and $z = 0$ (b) at different optimization steps n_{opt}.

compared to the global refinement case. The multilevel refinement algorithm, which is implemented in DROPS, makes it easy to use such locally refined triangulations. The solution of the considered IHCP on such grids remains a challenging task for future investigations. In this context, suitable error estimators have to be developed

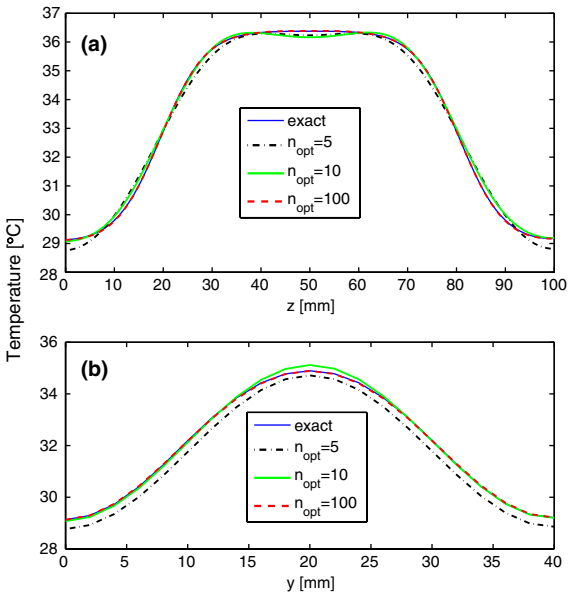

Fig. 13. 2D plots of the temperatures for $y = 0$ (a) and $z = 0$ (b) at different optimization steps n_{opt}.

that are based on the spatial behaviour of the unknown quantity, which is not the solution of the direct problems (i.e. the temperature distributions) but the corresponding boundary condition on Γ_2.

The temperature distributions corresponding to the estimated quantities are shown in Fig. 13(a) and (b) together with the exact values for different optimization steps. The plots show that we obtain high proximities to the exact temperature distributions after only few optimization iterations in contrast to the corresponding heat fluxes. This example shows, that the value of the functional is in general not a good measure for the quality of the estimation. The fit of the temperatures may be almost perfect, even though the estimated heat flux is quite different from the exact one. This largely unavoidable effect is due to the ill-posedness of inverse heat conduction problems caused by the strong smoothing properties of the direct problem.

6. Estimation results with measurement data

In this section, we present an estimation case study for the real falling film experiment employing the high resolution temperature measurements. These are taken with an IR camera on the back side Γ_1 of the constantan foil, which has a thickness of 25 μm. The main idea behind choosing a very small heating foil consists in reaching a small temperature gradient across the foil thickness, i.e. the temperatures on both sides of the foil should be nearly identical. In that case, the measured data will be a good estimate of the temperature on the inaccessible film side of the foil. The measurement section has the dimension $19.5 \times 39\ \mathrm{mm}^2$. Hence, we define the domain $\Omega := 0.025 \times 19.5 \times 39\ \mathrm{mm}^3$. Due to this geometric anisotropy, we have to use degenerated finite elements (see Section 4).

The measurement data are taken with a sampling frequency of 500 Hz and a space resolution of 100×200 pixel. These technical data translate to a time step size of $\tau = 2$ ms in the one step θ-scheme and a space discretization of 100×200 unknowns in the y–z-plane in the case of a one by one allocation, i.e. if we consider the same resolution for the measurement data and the numerical simulation. For the space discretization in the x-direction only five unknowns are used, which turns out to be an appropriate choice. To investigate the effect of the discretization in x-direction on the temperature profile, we solved the direct problem for five and nine unknowns, respectively. As no additional frequencies appeared using the finer space mesh, we conclude that already the coarser grid is appropriate for the resolution of the temperature changes in that direction. Altogether we get a space discretization with 472,824 tetrahedra. The final time of the experiment is $t_f = 0.3$ s, which corresponds to 150 temperature frames that are taken with the IR camera in order to observe the influence of some waves flowing off with the laminar falling film.

The electrical heating generates a constant heat flux $q_h(\mathbf{x}, t) = 6.4\ \mathrm{kW/m}^2$, $(\mathbf{x}, t) \in \Gamma_1 \times [t_0, t_f]$. For the initial approximation, we choose $q_c^0(\mathbf{x}, t) = q_h$, $(\mathbf{x}, t) \in \Gamma_2 \times [t_0, t_f]$, because we expect q_c and q_h to have the same order of magnitude, due to the very thin heating foil. The other boundaries of the space domain are assumed to be perfectly insulated and the initial temperature distribution corresponds to the first temperature frame assumed to be constant across the foil thickness. The material properties of the foil are

$$\rho = 8900\ \mathrm{kg/m}^3, \quad c = 410\ \mathrm{J/kgK}, \quad \lambda = 23\ \mathrm{W/mK}$$

resulting in a thermal diffusivity of $a = 6.3 \times 10^{-6}\ \mathrm{m}^2/\mathrm{s}$.

In Fig. 14 the measured temperature distribution over the y–z-plane at a certain point in time is shown. The plot clearly shows that these data are perturbed by a large amount of noise. Without going into more detail here, we mention the measurement preprocessing applied to the experimental data of the falling film. The convective heat transport in flow direction causes a constant rise of the film temperature of approximately 0.05 K/mm, which overlays the local fluctuations caused by the waves. In order to remove this effect of the convective heat transport in the flow direction, a reference picture is subtracted from all the temperature frames taken with the IR camera, which is the reason for the use of insulated boundary conditions in the flow direction.

A typical observation in the context of inverse problems deals with the effect of noise in the given input data with respect to the number of optimization iterations. Fig. 15 shows the evolution of the corresponding objective functional, which decreases rapidly in the first iterations and flattens in the following steps. Although the temperature residual gets smaller, the quality of the corresponding estimated heat flux gets worse because of oscillations that appear with a rising number of optimization steps. This is an important reason why we have to investigate suitable regularization methods.

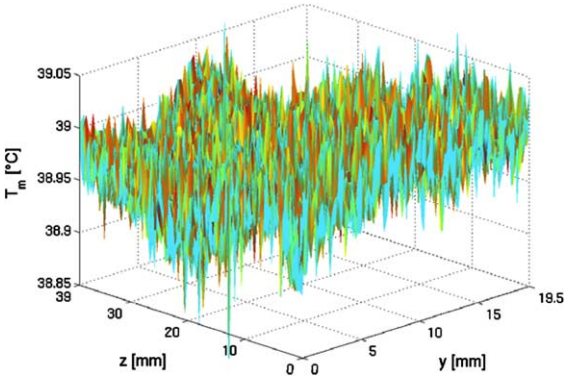

Fig. 14. Measured temperature data.

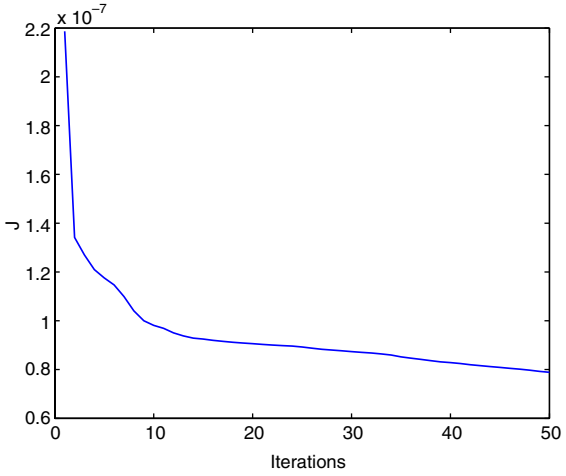

Fig. 15. Objective functional over iterations.

In Fig. 16, the optimal solution computed on the basis of measured input data is presented over the given time interval. Here, the estimated heat flux q_c^{15} is plotted for different time values. The discrepancy principle as described above has been used as a stopping rule resulting in $n_{\text{opt}} = 15$ iterations. The estimated standard deviation of the measurement error is $\sigma = 0.02$. As a reference for the quality of the calculated result the measured temperature and the calculated temperature are shown as well. The L-curve for this case is shown in Fig. 17. We see that the optimal estimate is also obtained after 15 iterations, though the maximum curvature point is not very much exposed.

Looking at the solution over the time interval we observe that the estimated heat flux shows a wavy structure moving along in the flow direction of the falling film (i.e. the z-direction) with the same frequency as the film waves. This can be traced back to the influence of the

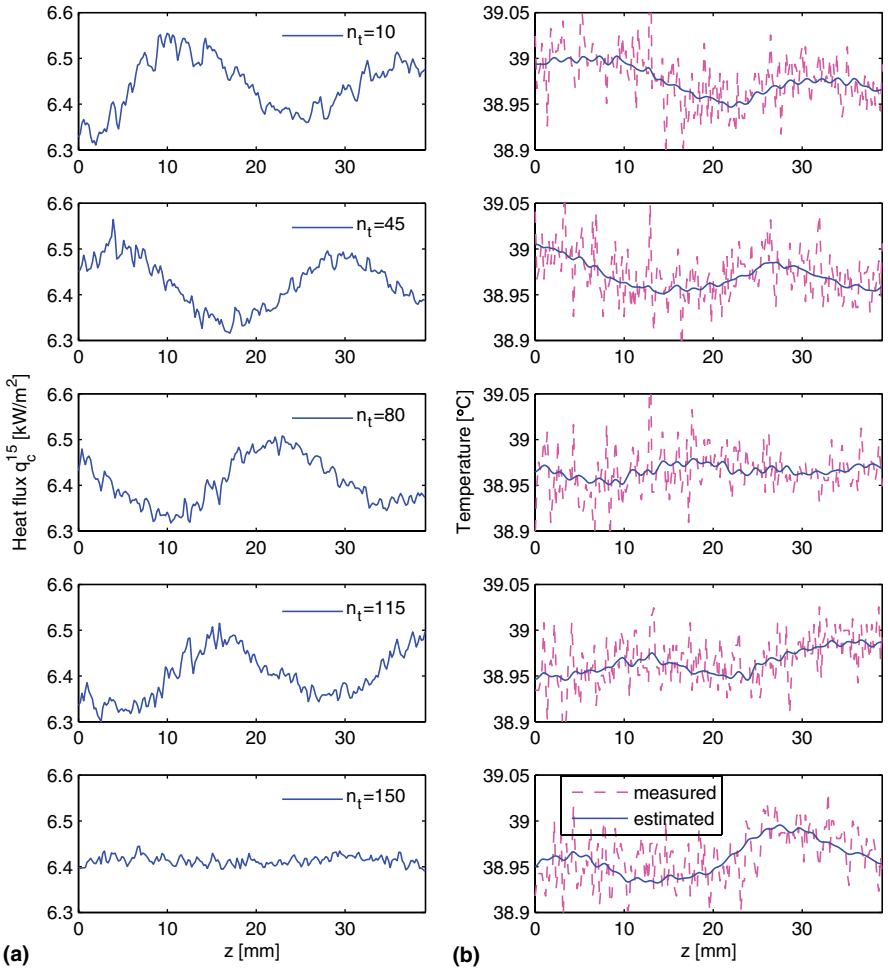

Fig. 16. Estimation result after 15 iterations at different time steps: heat flux estimate q_c^{15} (a), measured (dashed line) and estimated temperature (solid line) (b).

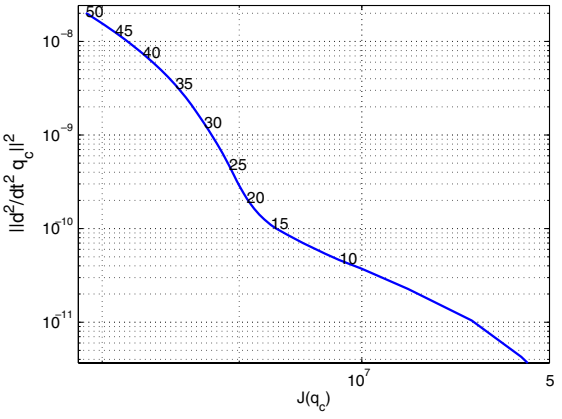

Fig. 17. L-curve for the measurement data.

wavy film surface whose varying thickness effects the amount of heat that is transferred from the foil to the film. The quality of the approximation decreases at the end of time, since the solution of the adjoint problem is zero at final time and therefore causes no improvement of the corresponding iterative solution.

7. Conclusions and future work

The conjugate gradient method has successfully been applied to the 3D transient inverse heat conduction problem in a falling film experiment to estimate the boundary heat flux at the film side of the heating foil from high resolution temperature measurements taken with an infrared camera at the foil back side. Simulation studies show that a time-dependent heat flux can be adequately predicted from the measurements within few iterations of the CG algorithm. The quality of the estimation depends on the level of the measurement error.

Future work will be devoted to the more complex problem of estimating the heat flux on the wavy surface of the falling film. For this task, we need to address momentum equations in addition to the energy equation including convective terms. The same algorithm can also be used for this case. Moreover, using the estimation procedure we can perform an optimal design of the experimental setup and determine conditions to enhance the information content of the measurements.

Acknowledgement

Financial support from DFG (Deutsche Forschungsgemeinschaft) via the collaborative research center SFB 540 and the graduate program GRK 775 is gratefully acknowledged.

References

[1] F. Al-Sibai, A. Leefken, U. Renz, Local and instantaneous distribution of heat transfer rates through wavy films, Int. J. Therm. Sci. 41 (2002) 658–663.
[2] O.M. Alifanov, Inverse Heat Transfer Problems, Springer, Berlin, 1994.
[3] U.M. Ascher, E. Haber, A multigrid method for distributed parameter estimation problems, Electron. Trans. Numer. Anal. 15 (2003) 1–17.
[4] I. Babuska, A.K. Aziz, On the angle condition in the finite element method, SIAM J. Numer. Anal. 13 (1976) 214–226.
[5] J.V. Beck, B. Blackwell, A. Haji-Sheikh, Comparison of some inverse heat conduction methods using experimental data, Int. J. Heat Mass Transfer 39 (17) (1996) 3649–3657.
[6] S. Chantasiriwan, An algorithm for solving multidimensional inverse heat conduction problems, Int. J. Heat Mass Transfer 44 (2001) 3823–3832.
[7] H.W. Engl, M. Hanke, A. Neubauer, Regularization of Inverse Problems, Kluwer Academic Publishers, Dordrecht, 1996.
[8] S. Gross, J. Peters, V. Reichelt, A. Reusken, The DROPS package for numerical simulations of incompressible flows using parallel adaptive multigrid techniques. Technical Report No. 211, IGPM, 2002. <http://www.igpm.rwth-aachen.de/reports/ps/IGPM211.ps.gz>.
[9] C. Hansen, Rank-Deficient and Discrete Ill-posed Problems: Numerical Aspects of LSIAM Inversion. SIAM Monographs, SIAM, Philadelphia, USA, 1998.
[10] G. Hetsroni, D. Mewes, C. Enke, M. Gurevich, A. Mosyak, R. Rozenblit, Heat transfer to two-phase flow in inclined tubes, Int. J. Multiphase Flow 29 (2) (2003) 173–194.
[11] G. Hetsroni, R. Rozenblit, Heat transfer to a liquid–solid mixture in a flume, Int. J. Multiphase Flow 20 (1994) 671–689.
[12] C.-H. Huang, S.-P. Wang, A three-dimensional inverse heat conduction problem in estimating surface heat flux by conjugate gradient method, Int. J. Heat Mass Transfer 42 (1999) 3387–3403.
[13] M. Krizek, On the maximum angle condition for linear tetrahedral elements, SIAM J. Numer. Anal. 29 (1992) 521–527.
[14] A. Leefken, F. Al-Sibai, U. Renz, Measurement of instantaneous heat transfer using a hot-foil infrared technique, in: Thermosense XXIII, Proceedings of SPIE, Orlando, USA, vol. 4630, April 16–19, 2001, pp. 21–29.
[15] S. Leuthner, A.H. Maun, S. Fiedler, H. Auracher, Heat and mass transfer in wavy falling films of binary mixtures, Int. J. Therm. Sci. 38 (1999) 937–943.
[16] T. Lüttich, A. Mhamdi, W. Marquardt, Design, formulation and solution of multi-dimensional inverse heat conduction problems, Numer. Heat Transfer: Part B: Fundamentals 47 (2) (2005) 111–133.
[17] T.H. Lyu, I. Mudawar, Statistical investigation of the relationship between interfacial waviness and sensible heat transfer to a falling liquid film, Int. J. Heat Mass Transfer 34 (5) (1991) 1451–1464.

[18] W. Marquardt, Model-based experimental analysis of kinetic phenomena in multi-phase reactive systems, Chem. Eng. Res. Des. 83 (A8) (2005) 1–13.
[19] K.W. Morton, D.F. Mayers, Numerical Solution of Partial Differential Equations, Cambridge University Press, Cambridge, New York, Melbourne, 1994.
[20] J. Nocedal, S.J. Wright, Numerical Optimization, Springer, Berlin, Heidelberg, New York, 1999.
[21] A. Quarteroni, A. Valli, Numerical Approximation of Partial Differential Equations, Springer, Berlin, Heidelberg, 1994.
[22] Y. Saad, Iterative Methods for Sparse Linear Systems, Second ed., SIAM, Philadelphia, PA, 2003.
[23] C. Yang, C. Chen, Inverse estimation of the boundary condition in three–dimensional heat conduction, J. Phys. D. Appl. Phys. 30 (15) (1997) 2209–2216.